iScience

CellPress
OPEN ACCESS

Article

Insights into electron wind force by a helical dislocation reconfiguration

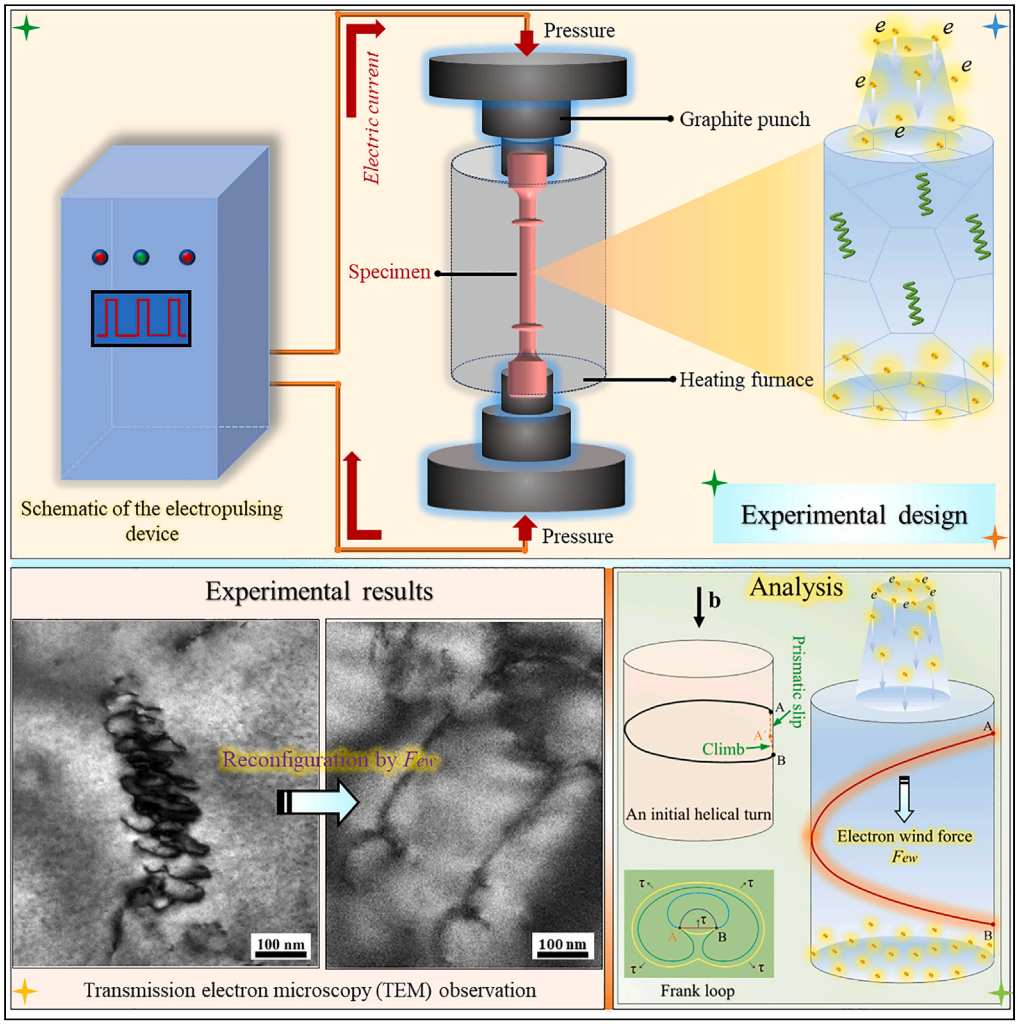

Chang Zhou, Lihua Zhan, Chunhui Liu, Minghui Huang

yjs-cast@csu.edu.cn

Highlights

An innovative experiment design and obtained results first verify electron wind force

Our findings exhibit a significant reconfiguration of an initial helix under EPT

Revealing the kinematics of an "opened out" process of a dislocation helix under *Few*

Zhou et al., iScience *26*, 106870
June 16, 2023
https://doi.org/10.1016/j.isci.2023.106870

iScience

CellPress
OPEN ACCESS

Article

Insights into electron wind force by a helical dislocation reconfiguration

Chang Zhou,[1] Lihua Zhan,[1,2,3,4,*] Chunhui Liu,[2,3] and Minghui Huang[2,3]

SUMMARY

Many efforts for decades have been made to explore electron wind force, produced by electric current itself under electropulsing treatment. However, the clear evidence of this force is hard to separate from Joule heating. Here we study a helical dislocation within quenched Al-Cu-Li alloy when subjected to a pulsed current. Such a helical configuration is quite suited for uncoupling this force from Joule heating effect because, contrary to general dislocations, it can take a unique reconfiguration under a driving force parallel to its Burgers vector. We find that within the pulsed samples, an initial helix happens to reconfigure, evolving into a line morphology. Therefore, it is this electron wind force F_{ew}, which parallel to the Burgers vector, would result in such novel helix reconfiguration when compared to the absence of this force. This is the first study to verify electron wind force by a helical dislocation reconfiguration.

INTRODUCTION

Electrical pulsing treatment (EPT) technique, introducing a pulsed current into a material without deformation, has been suggested to be a highly effective and promising method to tailor the microstructure of the materials.[1] Many research works for decades have been carried out on the EPT impacts on mechanical property,[2–7] phase transformation,[8–11] recrystallization,[12–16] and aging kinetics,[17–21] all of which involve the microstructure modifications. The application of electropulsing has been seen to result in an instantly decreased flow stress and a significantly increased elongation for tensile tests of the 5052-H32 aluminum alloy, which attributes to the dislocation annihilation via the athermal effects of electropulsing.[3] It was also reported that the recrystallization kinetics was accelerated by the EPT for AZ31 magnesium alloy, due to the reduced activation energy for recrystallization by around 60%.[14] The authors also reported that the markedly shortened aging process through EPT for the Al-Cu-Li alloy is due to the reduced average diffusion field size via the formation of dislocation network configuration induced by electropulsing.[18] These EPT studies commonly show that microstructural modification can be accelerated by the athermal effects produced by electric current itself, and further resulting in improvements of material property. While the existence of athermal effects of EPT is well established experimentally, its clear mechanism has not been identified until now. A most popular assumption to explain the athermal effect of EPT is suggested to be the electron wind force (F_{ew}), a direct force transmission from the drifting electrons onto the dislocations. Kravchenko[22] firstly proposed that high-speed drifting electrons are capable of exerting a force on the dislocations in the crystal lattice of the metals and also gave a theoretical formula of estimating this "electron wind" force. In Kravchenko theory, electron wind force could explain a non-thermal mechanism for the electroplasticity effect. It was grounded on the assumption of an equivalence of electrons effects on dislocations to mechanical forces and stresses. Later, both Klimov et al.[23] and Roschupkin et al.[24] provided a simplified expression for the electron wind force (F_{ew}) on the basis of Kravchenko's "electron wind" theory.

Kravchenko

$$\frac{F_{ew}}{l} = \left[\frac{b}{4}\left(\frac{3n}{2E_F}\right)\frac{\Delta^2}{v_F}\right](v_e - v_d) = \left(\frac{3b}{8}\frac{\Delta^2}{eE_F v_F}\right)J \qquad \text{(Equation 1)}$$

Klimov et al.

$$\frac{F_{ew}}{l} = \left[\frac{b}{4}\left(\frac{3n}{2E_F}\right)\frac{\Delta^2}{v_F}\right](v_e - v_d) = \left(\frac{3b}{8}\frac{\Delta^2}{eE_F v_F}\right)J \qquad \text{(Equation 2)}$$

[1]College of Mechanical and Electrical Engineering, Central South University, Changsha 410083, China

[2]State Key Laboratory of Precision Manufacturing for Extreme Service Performance, Central South University, Changsha 410083, China

[3]Light Alloys Research Institute, Central South University, Changsha 410083, China

[4]Lead contact

*Correspondence: yjs-cast@csu.edu.cn

https://doi.org/10.1016/j.isci.2023.106870

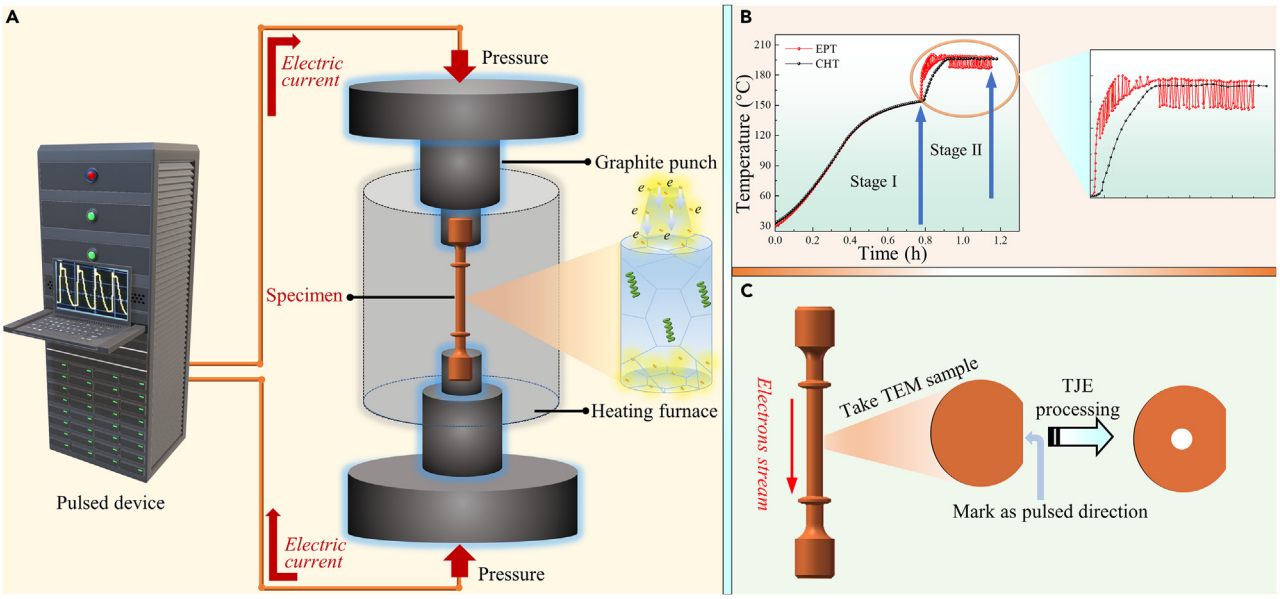

Figure 1. Experimental system of electrical pulsing treatment (EPT) and subsequent preparation method of TEM sample

(A) Schematic diagram of the EPT apparatus.

(B) Temperature history of the CHT and EPT samples and a magnification box on the right of temperature curves clearly showing the temperature rise when electropulsing was applied.

(C) The arc-shaped TEM sample was prepared in order to confirm the relationship between electron flux direction and dislocation distribution.

Roschupkin et al.

$$\frac{F_{ew}}{l} = \left[\frac{b}{4}\left(\frac{3n}{2E_F}\right)\frac{\Delta^2}{v_F}\right](v_e - v_d) = \left(\frac{3b}{8}\frac{\Delta^2}{eE_F v_F}\right)J \qquad \text{(Equation 3)}$$

where F_{ew}/l is the force per unit length acting on the dislocation, $v_e = J/en$ is the electron velocity, b is the Burgers vector, e is the electron charge, J is the current density, n is the electron density, m^* is the effective electron mass, E_F is the Fermi energy, v_F is the Fermi velocity, v_d is the dislocation velocity, and h is the Planck's constant. From these theoretical equations, the electron wind force is directly seen to be proportional to electron velocity. Furthermore, when assuming that dislocations are temporarily pinned by some obstacles (i.e., $v_d = 0$ here), this force is also proportional to the current density. Waryoba et al.[25] thought that electron wind force can specifically target the defective regions, which further results in the shortened processing time and the higher energy efficiency during the electrically treated annealing of metals. Recently, a report from Xiang et al.[26] indicated that electron wind force can enhance the movement of vacancies and also lead to dislocation rearrangement parallel to the direction of the drift electrons. Zhang et al.[27] by *in-situ* transmission electron microscopy (TEM) observations found that dislocations annihilation at first and then regeneration happen under the action of electron wind force. Recent work of Minor's team[28] demonstrated that enhancement of surface nucleation from electron wind force is more likely than Joule heating to be the origin of the more uniform plasticity observed during electrical pulsing. Besides, in the hypothesis of electron wind force, electric current density, which may trigger solute atoms to move, is required to be greater than 10^2-10^4 A/mm^2.[29,30] However, these current research works on electron wind are still under a hypothesis and are not capable of providing clear evidences of electron wind force due to the lack of the reliable experimental data.

Helical dislocations have been widely observed within the metals and alloys subjected to radiation damage, cold work, or quenching from high temperatures. In addition, the formation mechanism of this helical dislocation has been reported to be that defect-mediated climb for the screw component of dislocations in the irradiated materials.[31] For the quenched samples with an excess of vacancies, these helical dislocations with their axes parallel to the direction of Burgers vector <110> are suggested to arise from the vacancy-induced climb of screw dislocations.[32] Such dislocation structure with a specially helical character should be prone to take shape into a straight-line morphology when subjected to a driving force, whose direction

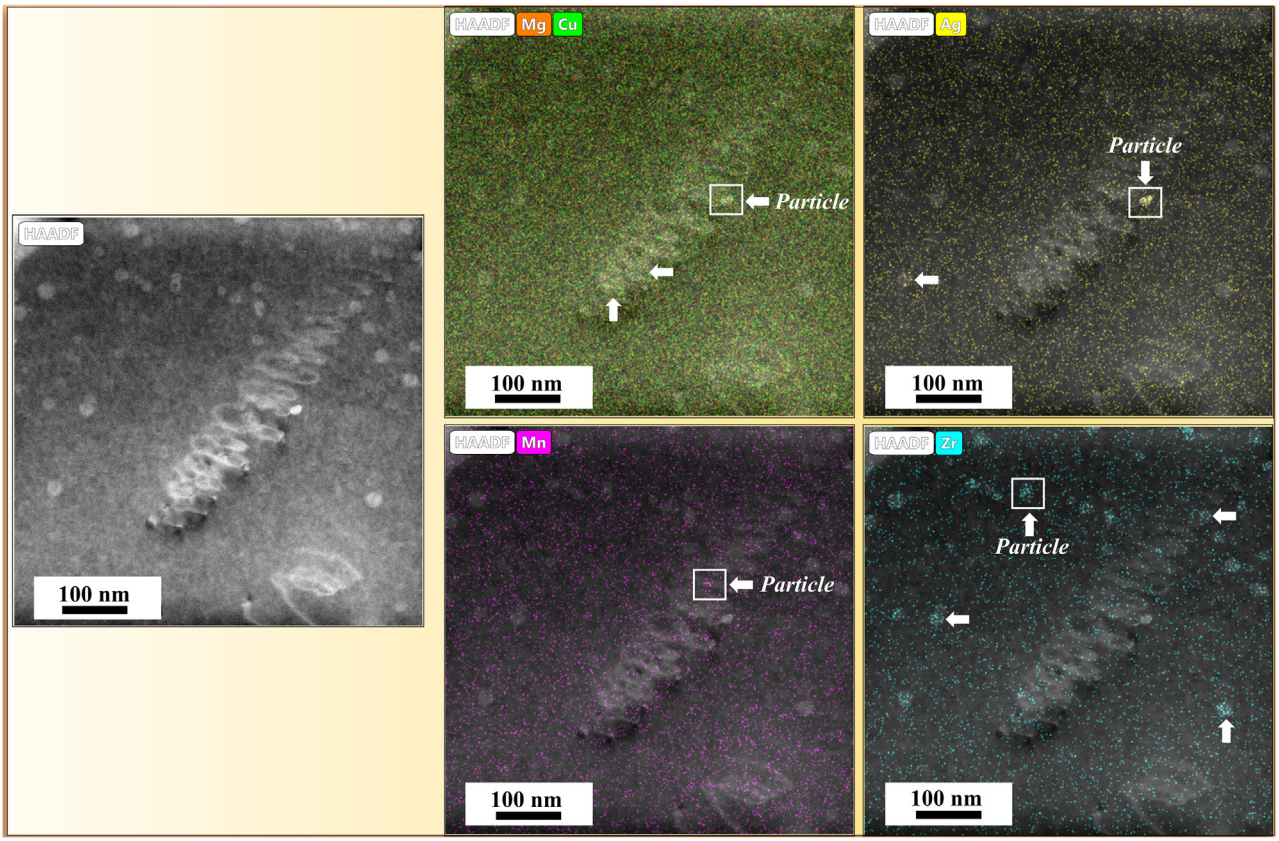

Figure 2. HAADF images and corresponding EDS STEM-Mapping of these particles
They exist around helical dislocations within the initial samples.

is consistent with the Burgers vector **b**. This special kind of helical dislocation was observed to only expand along the radial direction at thermally activated state.[33] If a helical dislocation happens to a significant reconfiguration, i.e., evolving into a straight-line morphology, we can firmly infer the presence of this electron wind force, when confirmed the consistent direction between electron flow and the axis of the helix. Therefore, this helical configuration is uniquely suited to uncouple the electron wind force from Joule heating during the EPT process. In other words, we can acquire clear and convincing pieces of evidence of electron wind force from helical dislocation reconfiguration in the EPT samples.

In the present work, we investigated evolution of the helical dislocations from the quenched Al-Cu-Li alloy under the EPT conditions, to reliably verify its predominant role of electron wind force. This helix structure is of a great interest in this context due to a pronounced reconfiguration when subjected to a driving force parallel to the Burgers vector. Namely this driving force is strongly considered as electron wind force when this parallel relationship between electron stream and the Burgers vector was confirmed during dislocation reconfiguration.

RESULTS AND DISCUSSION

Firstly, bright-field images of the stage I sample were observed to validate the helical configuration of dislocations produced by quenching. Figure 3 clearly shows the presence of uniquely helical configurations, with a bunch of successive turns. It should be emphasized that these dislocations seem to appear with ordered shape and specific orientation in the Al matrix. This direction-specific distribution is expected to be beneficial to study electrons wind force when high-speed electrons flow into dislocations along the pitch direction. In addition, an enlarged view in Figure 3 shows a clear dislocation helix with the absence of clusters or particles on it, which is on account of the pre-treatment of stage I. In order to further confirm this point, a high-angle annular dark-field (HAADF) image was also provided with the corresponding

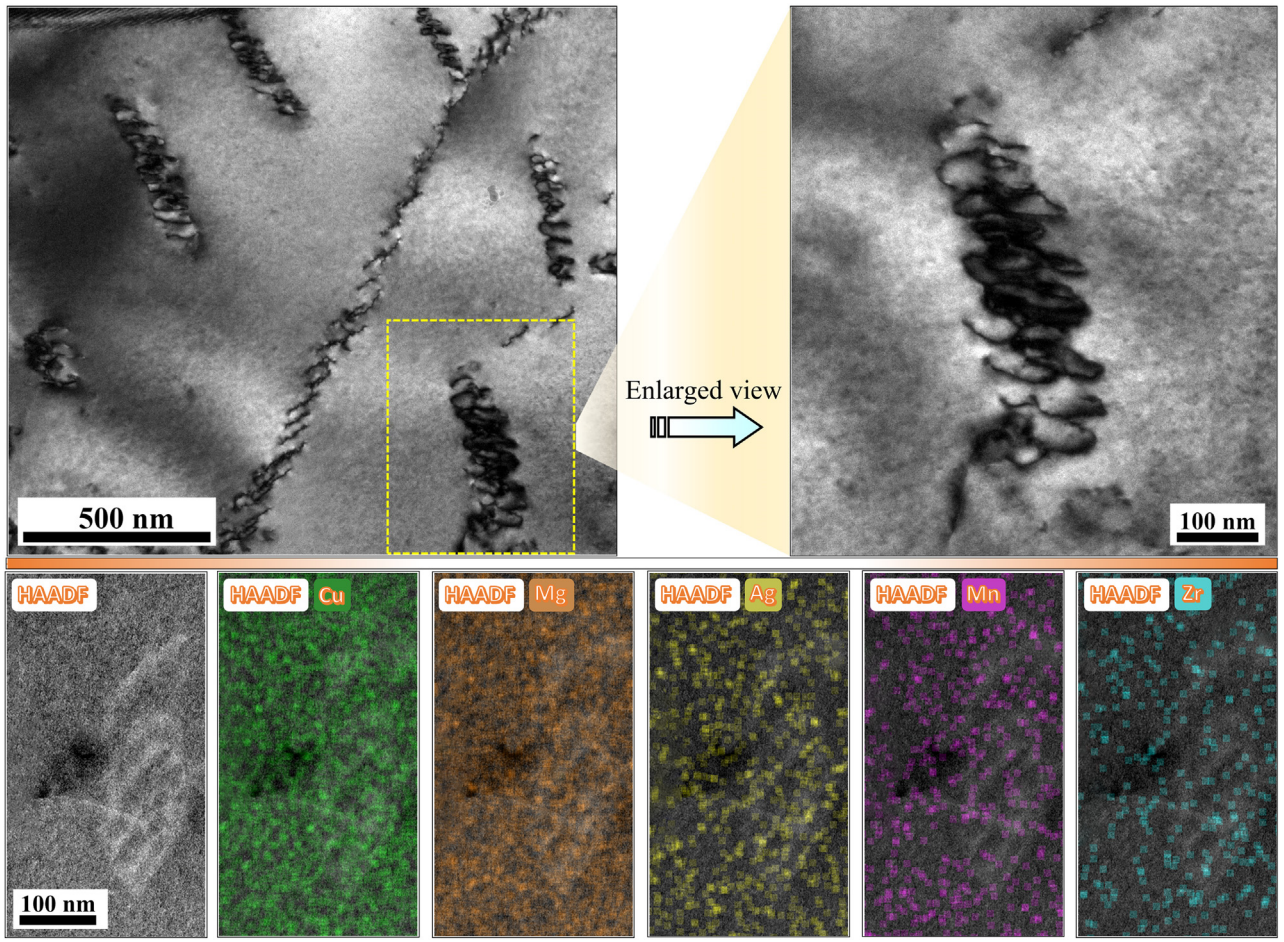

Figure 3. Microstructural characterization of the sample after Stage I

TEM bright-field images of the sample after stage I, clearly showing a uniquely helical configuration produced during the quenching. And a high-angle annular dark-field (HAADF) image of the stage I sample, with corresponding EDS mapping of different elements. It proves that none of clusters or particles exists around these helical dislocations after the stage I.

energy-dispersive x-ray spectroscopy (EDS) mapping of different elements in Figure 3. Results amply prove that none of clusters or particles, as mentioned in Figure 2, exists around these helical dislocations after the stage I. It means that these thermally activated helical dislocations (here defined as the initial dislocation) should be more prone to be triggered to move when subjected to a certain driving force.

In order to verify the hypothesis of predominant role of electrons wind force, we, therefore, specifically performed the observations of helical dislocation evolution after the EPT and conventional heat treatment (CHT) for various times. Firstly, we have confirmed by the method as mentioned in Figure 1C this almost parallel relationship between electron flow and the pitch direction of helical dislocation, as detailed in an image between (A) and (B) of Figure 4. These TEM observations revealed significant differences in dislocation configuration between the EPT and CHT samples. After EPT for 3 min, these helical dislocations were observed to reconfigure slightly, from an initially regular helix to a variant with a part of a straight line at the top end as shown in Figure 4A. This clearly suggests that an "opened out" process for a dislocation helix seems to be happening under a driving force parallel to the pitch direction, much presumably due to electrons wind force. A higher magnification in Figure 4B more clearly shows an evolved helical dislocation structure in the EPT sample for 3 min. With increasing time to 20 min, a sharp transition of a regular dislocation helix was found to happen into an almost opened helix structure. This evolutive process appears to that a helix with a string of tightly packed coils is gradually straightened, with the steadily increased pitch accompanied with the decreased turns, when subjected to a driving force. Apparently, a fully "opened out" dislocation helix, almost a straight line, is presented in Figure 4D. It should be noted that there is an obvious

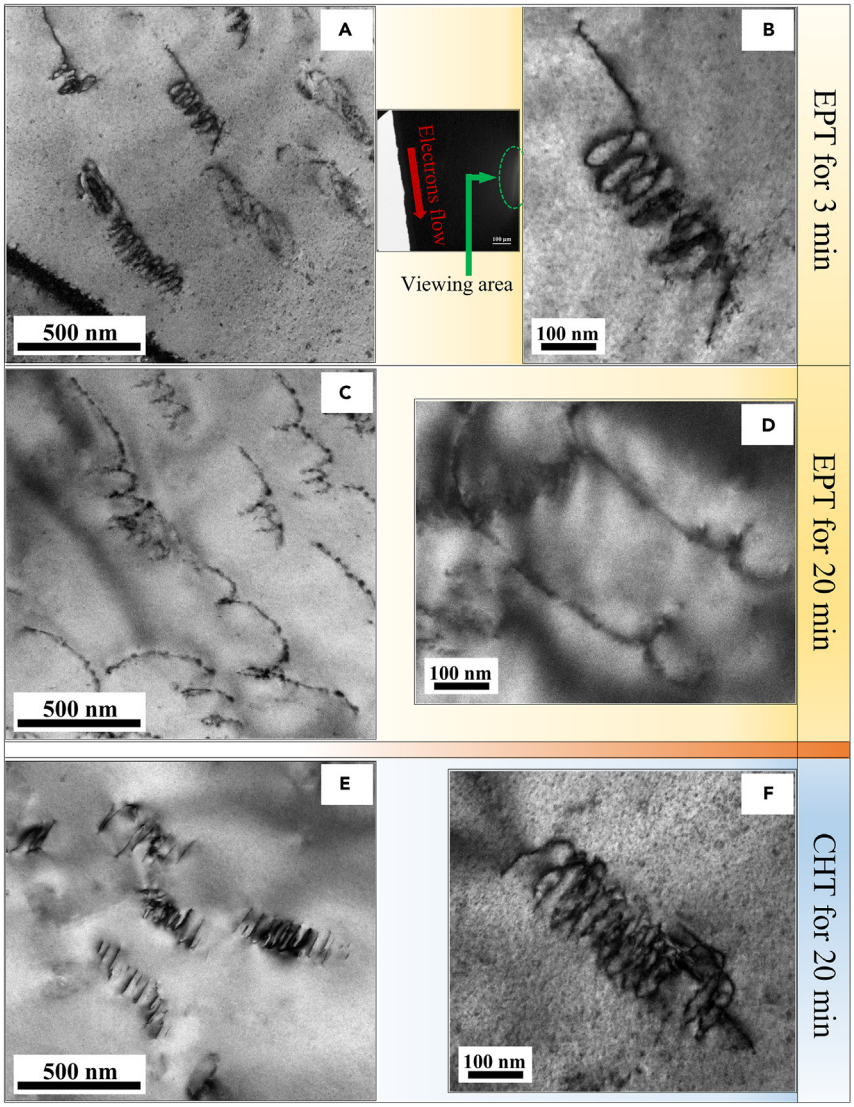

Figure 4. Bright-field TEM images of the EPT and CHT samples, showing the dislocation configuration under different conditions, respectively

(A–F) (A), (B) the EPT sample for 3 min; (C), (D) the EPT sample for 20 min; (E), (F) the CHT sample for 20 min. Note that we confirm this almost parallel relationship between electrons flow and the pitch direction of helical dislocation, as detailed in an image between (A) and (B).

expansion of helical turns along the radius direction when compared with that of an initial helix. However, these helical dislocations in the CHT sample for 20 min, as control group with the absence of electron flows, were almost similar with the initial dislocation helices but only with the increase in radius of helical turns as shown in Figures 4E and 4F. Therefore, electrons wind force formed by current itself can seem to be established via a great morphological difference of dislocations after the EPT and CHT all for 20 min, in that such an "opened out" process of dislocation helices is specific to the EPT sample with high-speed electron flows along the pitch direction.

To further verify the electrons wind force during such an "opened out" process of the dislocation helix, we also by the $\mathbf{g}\cdot\mathbf{b}$ method[34] carried out the determination of the Burgers vector $\mathbf{b}$ for a helical dislocation in the EPT sample. Three extra g-vector images in Figure 5 were used to confirm the Burgers vector $\mathbf{b}$ of a helical dislocation. In term of the $\mathbf{g}\cdot\mathbf{b}$ invisibility criterion, the Burgers vector of it was identified to be $\frac{1}{2}[0\bar{1}\,\bar{1}]$. Figure 5D clearly shows a parallel relation between its Burgers vector $\mathbf{b}$ and the axial direction

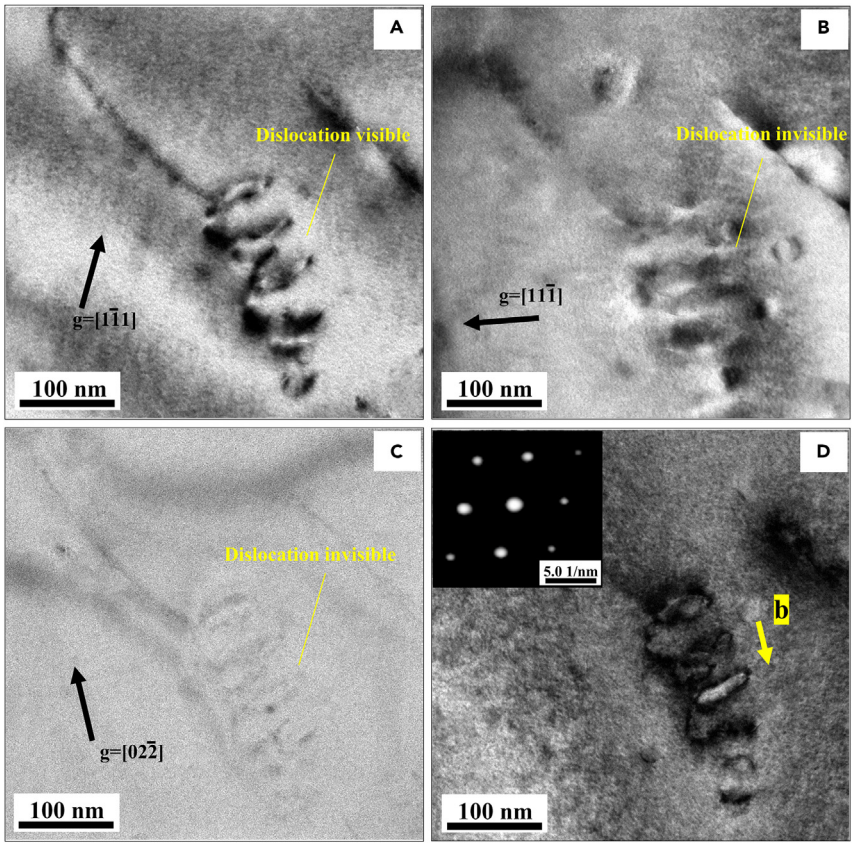

Figure 5. Characterization on the Burgers vector b of a helical dislocation

(A–C) A series of weak-beam bright-field micrographs (A)-(C), captured using several g-vectors. From the g b invisibility criterion, the helical dislocation has a Burgers vector of ½[0$\bar{1}\bar{1}$].

(D) showing the direction of the Burgers vector **b** (insert a diffraction pattern of [110] zone axis).

of a helical dislocation, which also agrees well with the results of the literature.[34,35] Consequently, the direction of electrons flow is almost consistent with the Burgers vector of the helical dislocations in the present case, which strongly means that it is the electron wind force that operates on the dislocation helix to induce its pronounced reconfiguration. So far, we have confirmed this indispensable and predominant role of electron wind force, by a reconfiguration of the uniquely dislocation helix during the EPT process.

Lastly, we further investigated the kinematics of an initially helical dislocation when subjected to the electron wind force. To study the detailed kinematics of a dislocation helix under electron wind force, we simplistically chose a helical turn AB as a research unit in Figure 6. The edge component A'B, arising from its projection on the climb plane normal to the Burgers vector **b**, was considered to possess the nature of a Frank loop. In this study, the climb force $\boldsymbol{\tau}$ of an edge component was mainly offered by the osmotic force F_{osm}, whose magnitude value is determined by vacancy concentrations.[36,37] As the vacancy diffusion controls climb of an edge component, the larger climb force $\boldsymbol{\tau}$ would form during stage II of the EPT condition. These increased free vacancies, owing to the temperature rise during the stage II, prefer to migrate into the helical dislocations acting as the vacancy-biased sinks, which can further lead to the increased vacancy concentration around helical dislocations. An edge component A'B will be driven to climb under this climb force $\boldsymbol{\tau}$, whose moving direction is normal to the Burgers vector **b**. This behavior can only lead to a steady expansion of helical turns with the nature of a Frank loop. Most importantly, the electron wind force F_{ew}, whose direction is almost along with the Burgers vector **b**, operates on the screw component AA' of a helical dislocation and promotes its prismatic slip (In Figure 6). According to the Equation 2, the electron wind stress τ_{ew} ($\tau_{ew} = F_{ew}/l$ here) is calculated as 15.0 Pa at the given current parameters of this work. We can also infer that this magnitude value of electron wind force F_{ew} is much sufficiently capable of triggering the slip of the screw component AA' on the surface of the cylinder with an axis parallel to its Burgers vector. This

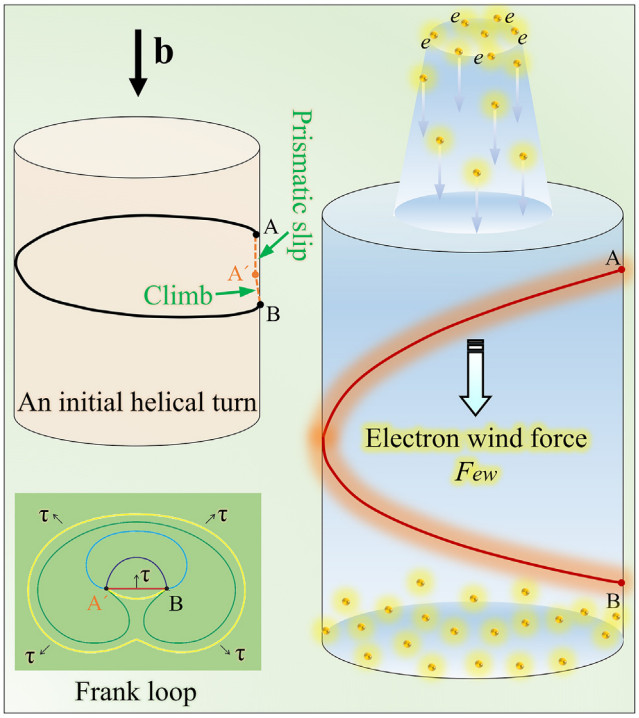

Figure 6. Schematic diagram of the kinematics for a helical dislocation under the electron wind force
It is worth noting that the electron wind force is consistent to the Burgers vector **b**.

inference is mainly based on a precondition that these helical dislocations were thermally activated state, as presented in this work. Moreover, it is such a beneficial prismatic slip of a screw component that will lead to the increasing space between spirals and further to straighten a dislocation helix. From the aspect of kinematics, an initial dislocation helix would take an "opened out" process with the combination of prismatic slip of the screw component and climb of the edge component during the EPT. It should be emphasized that this prismatic slip induced by electron wind force plays an indispensable and predominant role during a dislocation reconfiguration observed here.

Conclusions

In summary, we studied evolution of a dislocation helix, which is uniquely suited to verify the electron wind force produced by current itself under EPT conditions, in that such a helix line will be straightened when subjected to a driving force parallel to the Burgers vector **b**. This is the first study to verify the electron wind force by a helical dislocation reconfiguration. Our findings have shown that an initial dislocation helix took a clear and significant reconfiguration into a similarly straight line in the EPT sample. We have also confirmed that the direction of electron wind force is almost consistent with the Burgers vector of a helical dislocation in this work. Finally, we have also revealed the kinematics of an "opened out" process of a dislocation helix when subjected to the electron wind force. This work, which designs an innovative experiment of a helical dislocation reconfiguration, will provide new insights into the electron wind force in the EPT field.

Limitations of the study

In this study, we proposed a kind of innovative experimental design, i.e., a helical dislocation reconfiguration via electropulsing and then verified the existence of electron wind force. However, real-time observation of a helical dislocation evolution is not very detailed under electropulsing. Our subsequent study will focus on the entire evolution process of it via *in-situ* TEM.

STAR★METHODS

Detailed methods are provided in the online version of this paper and include the following:

- KEY RESOURCES TABLE

ACKNOWLEDGMENTS

This work was financially supported by the National Natural Science Foundation of China (U22A20190); the Science and Technology Innovation Program of Hunan Province (2020RC4001); National Natural Science Foundation of China (51601060).

AUTHOR CONTRIBUTIONS

Chang Zhou: Conceptualization, investigation, writing – original draft. Lihua Zhan: Conceptualization, funding acquisition, writing – review & editing. Chunhui Liu: supervision, writing – review & editing. Minghui Huang: supervision, writing – review & editing.

DECLARATION OF INTERESTS

The authors declare that they have no conflict of interests.

Received: October 10, 2022
Revised: February 20, 2023
Accepted: May 10, 2023
Published: May 12, 2023

REFERENCES

1. Liang, C.L., and Lin, K.L. (2018). The microstructure and property variations of metals induced by electric current treatment: a review. Mater. Char. *145*, 545–555. https://doi.org/10.1016/j.matchar.2018.08.058.

2. Qin, S., Hao, J., Yan, L., and Zhang, X. (2021). Ultrafast solution treatment to improve the comprehensive mechanical properties of superalloy by pulsed electric current. Scripta Mater. *199*, 113879. https://doi.org/10.1016/j.scriptamat.2021.113879.

3. Roh, J.H., Seo, J.J., Hong, S.T., Kim, M.J., Han, H.N., and Roth, J.T. (2014). The mechanical behavior of 5052-H32 aluminum alloys under a pulsed electric current. Int. J. Plast. *58*, 84–99. https://doi.org/10.1016/j.ijplas.2014.02.002.

4. Kumar, A., and Paul, S.K. (2021). Improvement in tensile properties of pre-strained steel specimen by applying pulsed electric current. Materialia *15*, 100960. https://doi.org/10.1016/j.mtla.2020.100960.

5. Xiao, H., Xia, X., Huang, S., Chen, Q., Zhao, G., Zhao, Z., Wang, Y., Chai, S., and Peng, F. (2022). Study on mechanical behavior and microstructure evolution of Al-Mg-Li alloy during electropulsing assisted uniaxial tensile. J. Alloys Compd. *900*, 163425. https://doi.org/10.1016/j.jallcom.2021.163425.

6. Rudolf, C., Goswami, R., Kang, W., and Thomas, J. (2021). Effect of electric current on the plastic deformation behavior of pure copper, iron, and titanium. Acta Mater. *209*, 116776. https://doi.org/10.1016/j.actamat.2021.116776.

7. Chen, K., Zhan, L., Xu, Y., Ma, B., Zeng, Q., and Luo, S. (2022). Optimizing strength and ductility in 7150 Al alloys via rapid electropulsing cyclic heat treatment. J. Alloys Compd. *903*, 163985. https://doi.org/10.1016/j.jallcom.2022.163985.

8. Conrad, H. (2000). Effect of electric current on solid state phase transformations in metals. Mater. Sci. Eng. *287*, 227–237. https://doi.org/10.1016/S0921-5093(00)00780-2.

9. Zhou, Y.Z., Zhang, W., Guo, J., and He, G. (2006). Diffusive phase transformation in a Cu–Zn alloy under rapid heating by electropulsing. Phil. Mag. Lett. *84*, 341–348. https://doi.org/10.1081/09500830410001664535.

10. Zhang, X.F., Lu, W.J., and Qin, R.S. (2013). Removal of MnS inclusions in molten steel using electropulsing. Scripta Mater. *69*, 453–456. https://doi.org/10.1016/j.scriptamat.2013.05.033.

11. Jiang, Y., Tang, G., Shek, C., Zhu, Y., and Xu, Z. (2009). On the thermodynamics and kinetics of electropulsing induced dissolution of β-Mg17Al12 phase in an aged Mg-9Al-1Zn alloy. Acta Mater. *57*, 4797–4808. https://doi.org/10.1016/j.actamat.2009.06.044.

12. Fabrègue, D., Mouawad, B., and Hutchinson, C.R. (2014). Enhanced recovery and recrystallization of metals due to an applied current. Scripta Mater. *92*, 3–6. https://doi.org/10.1016/j.scriptamat.2014.07.004.

13. Jeong, K., Jin, S.W., Kang, S.G., Park, J.W., Jeong, H.J., Hong, S.T., Cho, S.H., Kim, M.J., and Han, H.N. (2022). Athermally enhanced recrystallization kinetics of ultra-low carbon steel via electric current treatment. Acta Mater. *232*, 117925. https://doi.org/10.1016/j.actamat.2022.117925.

14. Park, J.W., Jeong, H.J., Jin, S.W., Kim, M.J., Lee, K., Kim, J.J., Hong, S.T., and Han, H.N. (2017). Effect of electric current on recrystallization kinetics in interstitial free steel and AZ31 magnesium alloy. Mater. Char. *133*, 70–76. https://doi.org/10.1016/j.matchar.2017.09.021.

15. Liu, Y., Fan, J., Zhang, H., Jin, W., Dong, H., and Xu, B. (2015). Recrystallization and microstructure evolution of the rolled Mg-3Al-1Zn alloy strips under electropulsing treatment. J. Alloys Compd. *622*, 229–235. https://doi.org/10.1016/j.jallcom.2014.10.062.

16. Li, X., Li, X., Zhu, J., Ye, X., and Tang, G. (2016). Microstructure and texture evolution of cold-rolled Mg-3Al-1Zn alloy by electropulse treatment stimulating recrystallization. Scripta Mater. *112*, 23–27. https://doi.org/10.1016/j.scriptamat.2015.09.001.

17. Wang, Y., Chen, G., Chen, Z., Wan, H., Xiao, H., and Chang, X. (2022). Electropulsing assisted aging with ultrafast hardening rate for AerMet100 steel. Mater. Sci. Eng. *841*, 143066. https://doi.org/10.1016/j.msea.2022.143066.

18. Zhou, C., Zhan, L., Li, H., Chen, F., Liu, G., and Yan, D. (2021). Mechanism of an acceleration in T_1 precipitation kinetics in an Al-Cu-Li alloy by electropulsing. Vacuum *194*, 110558. https://doi.org/10.1016/j.vacuum.2021.110558.

19. Kapoor, R., Sunil, S., Bharat Reddy, G., Nagaraju, S., Kolge, T.S., Sarkar, S.K., Sarita Biswas, A., Biswas, A., and Sharma, A. (2018). Electric current induced precipitation in maraging steel. Scripta Mater. *154*, 16–19. https://doi.org/10.1016/j.scriptamat.2018.05.013.

20. Xu, X., Zhao, Y., Ma, B., and Zhang, M. (2014). Rapid precipitation of T-phase in the 2024 aluminum alloy via cyclic electropulsing treatment. J. Alloys Compd. *610*, 506–510. https://doi.org/10.1016/j.jallcom.2014.05.063.

21. Xiao, H., Jiang, S., Shi, C., Zhang, K., Lu, Z., and Jiang, J. (2019). Study on the microstructure evolution and mechanical properties of an Al-Mg-Li alloy aged by electropulisng assisted ageing processing. Mater. Sci. Eng. *756*, 442–454. https://doi.org/10.1016/j.msea.2019.04.049.

22. Kravchenko, V.Y. (1967). Effect of directed electron beam on moving dislocations. Sov. Phys. JETP *24*, 1135–1142.

23. Klimov, K.M., Shnyrev, G.D., and Novikov, I.I. (1975). Electroplasticity of metals. J. Sov. Phys. Dokl. *19*, 787–788.

24. Roshchupkin, A.M., Miloshenko, V.E., and Kalinin, V.E. (1979). Effect of electrons on the motion of dislocations in metals. J. Exp. Theor. Phys. Lett. *29*, 435.

25. Waryoba, D., Islam, Z., Wang, B., and Haque, A. (2019). Low temperature annealing of metals with electrical wind force effects. J. Mater. Sci. Technol. *35*, 465–472. https://doi.org/10.1016/j.jmst.2018.09.069.

26. Xiang, S., and Zhang, X. (2019). Dislocation structure evolution under electroplastic effect. Mater. Sci. Eng. *761*, 138026. https://doi.org/10.1016/j.msea.2019.138026.

27. Zhang, X., Long, Y., Huang, J., Xia, J., Gao, J., and Shao, G. (2020). Electron force-induced dislocations annihilation and regeneration of a superalloy through electric in-situ transmission electron microscopy observations. Rice *13*, 79–83. https://doi.org/10.1016/j.jmst.2019.08.008.

28. Li, X., Turner, J., Bustillo, K., and Minor, A.M. (2022). In situ transmission electron microscopy investigation of electroplasticity in single crystal nickel. Acta Mater. *223*, 117461. https://doi.org/10.1016/j.actamat.2021.117461.

29. Antolovich, S.D., and Conrad, H. (2004). The effects of electric currents and fields on deformation in metals, ceramics, and ionic materials: an interpretive survey. Mater. Manuf. Process. *19*, 587–610. https://doi.org/10.1081/LMMP-200028070.

30. Conrad, H. (2000). Electroplasticity in metals and ceramics. Mater. Sci. Eng. *287*, 276–287. https://doi.org/10.1016/S0921-5093(00)00786-3.

31. Amelinckx, S., Bontinck, W., Dekeyser, W., and Seitz, F. (1957). On the formation and properties of helical dislocations. Philos. Mag. A *2*, 355–378. https://doi.org/10.1080/14786435708243825.

32. Hellström, A., and Vingsbo, O. (1975). A quantitative tem investigation of helical dislocations in quenched Al-Cu alloys. Acta Metall. *23*, 1511–1514. https://doi.org/10.1016/0001-6160(75)90161-3.

33. Liu, C., Malladi, S.K., Xu, Q., Chen, J., Tichelaar, F.D., Zhuge, X., and Zandbergen, H.W. (2017). In-situ STEM imaging of growth and phase change of individual $CuAl_x$ precipitates in Al alloy. Sci. Rep. *7*, 2184. https://doi.org/10.1038/s41598-017-02081-9.

34. Haley, J.C., Liu, F., Tarleton, E., Cocks, A.C.F., Odette, G.R., Lozano-Perez, S., and Roberts, S.G. (2019). Helical dislocations: observation of vacancy defect bias of screw dislocations in neutron irradiated Fe–9Cr. Acta Mater. *181*, 173–184. https://doi.org/10.1016/j.actamat.2019.09.031.

35. Mizuno, K., Morikawa, K., Okamoto, H., and Hashimoto, E. (2014). Row of dislocation loops as a vacancy source in ultrahigh-purity aluminum single crystals with a low dislocation density. Trans. Mat. Res. Soc. Japan *39*, 169–172. https://doi.org/10.14723/tmrsj.39.169.

36. Liu, F.Z., Wang, D.W., Zhang, Y.J., Lv, Z.Y., Sun, X.D., Li, K.Y., Zhang, B., Wang, X.M., and Cui, F.Z. (2017). Numerical investigations of helical dislocations based on coupled glide-climb model. Int. J. Plast. *28*, 2–18. https://doi.org/10.1016/j.ijplas.2017.02.015.

37. Lothe, J., and Hirth, J.P. (1967). Dislocation climb forces. J. Appl. Phys. *38*, 845–848. https://doi.org/10.1063/1.1709423.

STAR★METHODS

KEY RESOURCES TABLE

REAGENT or RESOURCE	SOURCE	IDENTIFIER
Chemicals, peptides, and recombinant proteins		
Methanol/Methyl Alcohol	Katayama Chemical	CAS 64-17-5
Ethanol/Ethyl Alcohol	Nihon Shiyaku Reagent	CAS 67-56-1
Nitric Acid (61%)	Katayama Chemical	CAS 7697-37-2
Software and algorithms		
Digital Micrograph Software	AMETEK GATAN	https://www.gatan.com/products/temanalysis/digitalmicrograph-software
OriginLab 2019	OriginLab	https://www.originlab.com/2019
Other		
Transmission electron microscope (Talos F200X G2 TEM)	Thermo Fisher	https://www.thermofisher.cn/cn/zh/home/electronmicroscopy/products/transmissionelectron-microscopes/talos-f200xtem.html

RESOURCE AVAILABILITY

Lead contact

Further information and requests for resources should be directed to and will be fulfilled by the lead contact, Professor Lihua Zhan (yjs-cast@csu.edu.cn).

Materials availability

This study did not generate new materials.

Data and code availability

Data: The data that support the findings of this study are available from the authors on reasonable request. See author contributions for specific datasets.

Code: This paper does not report code.

For any additional questions or information please contact the lead contact.

EXPERIMENTAL MODEL AND SUBJECT DETAILS

This study does not involve experimental model or subject details.

METHOD DETAILS

Preparation method of materials

The AA2195 alloy with the chemical composition of Al-4.34Cu-0.95Li-0.33Mg-0.28Ag-0.15Zr (wt %) was used in this study. The dog bone-shaped specimen with a gauge length of 82 mm and 5 mm diameter, was machined along the roll direction from the as-received sheet, as shown in Figure 1A. All specimens were first given a solution treatment for 40 min at 510 °C, then water quenched and finally naturally aged for a week before the EPT.

Pre-treatment of the experimental samples

Given that the initial helical dislocations being pinned by these particles (see Figure 2 for details) formed during naturally aging after quenching, all samples firstly experienced a Stage I, in which heated from the room temperature to 155 °C by a furnace with a rate of 5 °C/min. This pre-treatment of Stage I would enable these particles to reversion into Al matrix, and further result in the thermal activation of dislocations.

Experimental procedures under EPT

After the Stage I, two kinds of heating process were respectively carried out through the EPT (as shown in Figure 1A) and the conventional heat treatment (CHT) using a furnace at the almost identical time-temperature history (Figure 1B) with EPT (here defined as Stage II). Herein the CHT test as a control group, was performed to exclude the Joule heating effect of electropulsing. It is pointed out that a TP700 temperature measuring device, with a K-type thermocouple, was used to record the temperature history between the gauge length of the specimens. Its measuring error is about ± 0.05 °C.

Parameters of pulsed currents

The pulsed current in this work, with a maximum current density of 26.5 A/mm^2, a pulse width of 1.3 ms and a period of 10 ms, produced a temperature rise of around 40 °C during the Stage II for 20 min. Note that this ratchet-shaped temperature curve for the EPT sample is due to the characteristics of the pulsed current, i.e., in each pulse period, the temperature instantly increases when applied a pulse and then rapidly decreases until the next pulse of electric current.

TEM characterization measurement

All TEM samples for helical dislocation analysis were taken at the center of the EPT specimen in terms of gauge length. TEM samples were firstly cut from the CHT and EPT specimens, then mechanically thinned to about 50 μm and punched into discs of 3 mm in diameter. Next these TEM samples were prepared by twin-jet electropolishing using a solution of 80% Methanol and 20% Nitric Acid at −30 °C and 15 V. Then these prepared TEM samples were cleaned by Ethanol. For the helical dislocation observation by TEM, it is worth noting that thin foils of the EPT sample were prepared as 3 mm diameter disk with a missing part as shown in Figure 1C, in order to mark the electron stream direction. Bright TEM imaging was performed using a Tecnai G2 T20 microscope operating at 200 kV.

QUANTIFICATION AND STATISTICAL ANALYSIS

This study does not involve quantification or statistical analysis.